Journal of
Manufacturing and Materials Processing

MDPI

Article

Modelling Machine Tools using Structure Integrated Sensors for Fast Calibration

Benjamin Montavon *, Philipp Dahlem, Martin Peterek, Markus Ohlenforst and Robert H. Schmitt

Laboratory for Machine Tools and Production Engineering (WZL) of RWTH Aachen University, 52074 Aachen, Germany; p.dahlem@wzl.rwth-aachen.de (P.D.); m.peterek@wzl.rwth-aachen.de (M.P.); m.ohlenforst@wzl.rwth-aachen.de (M.O.); r.schmitt@wzl.rwth-aachen.de (R.H.S.)

* Correspondence: b.montavon@wzl.rwth-aachen.de; Tel.: +49-241-80-20576

Received: 26 January 2018; Accepted: 18 February 2018; Published: 23 February 2018

Abstract: Monitoring of the relative deviation between commanded and actual tool tip position, which limits the volumetric performance of the machine tool, enables the use of contemporary methods of compensation to reduce tolerance mismatch and the uncertainties of on-machine measurements. The development of a primarily optical sensor setup capable of being integrated into the machine structure without limiting its operating range is presented. The use of a frequency-modulating interferometer and photosensitive arrays in combination with a Gaussian laser beam allows for fast and automated online measurements of the axes' motion errors and thermal conditions with comparable accuracy, lower cost, and smaller dimensions as compared to state-of-the-art optical measuring instruments for offline machine tool calibration. The development is tested through simulation of the sensor setup based on raytracing and Monte-Carlo techniques.

Keywords: volumetric performance; machine tool calibration; interferometry; cameras; raytracing; Gaussian laser

1. Introduction

At any given functional point within the working space of a machine tool, a relative deviation between the desired and actual tool tip position is expected. This is due to various error sources, such as for instance dynamic forces, thermo-mechanical deformations, unconsidered loads, the shortcomings of motion control, and inherent kinematic errors [1]. The upper limit of the resulting deviation per axis is defined as volumetric accuracy, and determines the volumetric performance [2]. Insufficient volumetric performance can be a cause of tolerance mismatch and should hence be avoided. This can be achieved for non-dynamic and repeatable influences by calibrating the machine tool and then compensating the known error motions via the motion control system. As previously mentioned, error sources are likely to vary over time and the calibration should be repeated regularly. Different techniques currently exist, and can be subdivided in methods using calibrated artifacts, e.g., ball-plates, and optical methods, e.g., interferometric multilateration [1,3].

All methods have two major drawbacks in common. Firstly, the production process has to be interrupted and the setup prepared for calibration, which means an unfavourable expenditure of time. Moreover, as defined in ISO 230-1:2012(en), the machine is calibrated under a »no-load or quasi-static condition« and may show significantly different behaviour compared to normal use during manufacturing [2]. The authors' concept is to (permanently) integrate optical sensors into the machine tool's axes, which in contrast to traditional scales are also capable of measuring transversal and angular movements of the axes' slides. This concept addresses the described drawbacks and will be presented in this paper. The complete idea is described for three-axis Cartesian machine tools and reduced to the measurement of error motions for a single axis. Thereafter, a specific hardware layout for integration is

described. In Section 4, the use of industrial cameras instead of quadrant detectors for the measurement of lateral laser beam displacement is suggested. This concept is implemented in a prototype, which is used for competitive measurements in Section 6.

2. The Concept of Integrated Optical Sensors for Three-Axis Machine Tool Calibration

The first underlying assumption of the elaborated concept is that all components of a three-axis Cartesian machine tool can be modelled as rigid bodies. Thus, the resulting deviation at the functional point can be stated as a superposition of contributions from the linear axes' individual error motions and squareness relations [4]. As a rigid body, every axis slide has six degrees of freedom for error motions: one linear positioning error motion parallel to the direction of motion, two perpendicular straightness error motions, and three angular error motions denominated yaw, pitch, and roll [2].

Hence, the calibration of the machine tool is reduced to the calibration of its linear axes and the application of a mathematical model according to the structural loop. This leads to the second fundament of the concept: If a sufficiently compact setup capable of measuring all error motions is integrated into the axes, the calibration setup can be made permanent without obstructing the working volume. There is no need to change the tool for an optical component, e.g. a reflector, and the measurement may be performed in a short time while the machine tool is not being used or even during operation. Using environmental compensation for optical measurements, the thermal behaviour of the axes can also be monitored by repeating the measurement sequence if the environmental conditions are expected to vary [5]. In the current state of the project, squareness errors between axes are excluded, which are especially inappropriate for large machine tools. In the future, the authors aim to slightly modify the individual base and head units using mirrors, pentaprisms, and beamsplitters, such that the visible laser propagates from a single source along the kinematic chain of the machine tool, serving as optical reference frame.

Figure 1 shows a sketch of the concept for a three-axis Cartesian machine of a gantry type. This machine type was chosen as a test carrier for a first implementation, but the application of the concept to any configuration of accessible linear axes is possible. At least one measurement line per direction of movement must be installed if the sensor setup is capable of measuring all error motions simultaneously. For this purpose, the layouts discussed in Section 3 are suitable. Their complexity can be reduced if multiple measurement lines (sketched in Figure 1 as dashed lines) are used, as angular movements can be calculated from the difference in linear movements. It is assumed that angular motions are of a small absolute value so that trigonometric functions can be approximated to the linear order of their Taylor series expansions. The calculation of the total deviation based on the axes' individual contributions is state-of-the-art and not further discussed here, and nor is the data processing in the motion control unit [6].

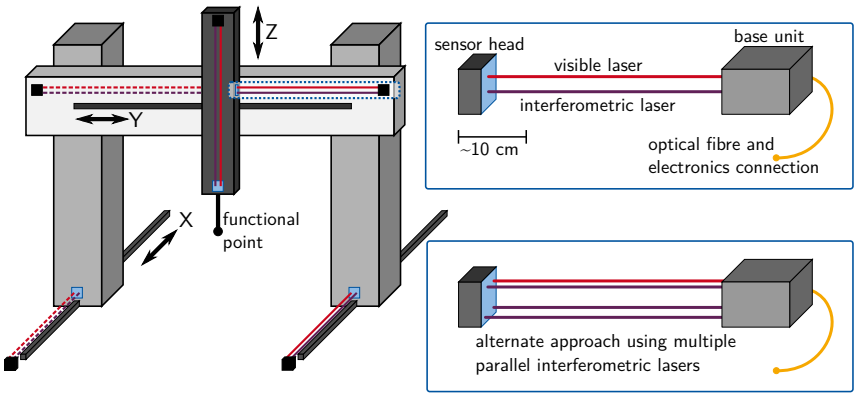

Figure 1. Schematic drawing of the idea to equip a three-axis machine of a gantry type with structure integrated sensors. The sensor head is the mobile part of the setup and is attached to the axis slide. The concept assumes strict rigid body behaviour of the machine tool and the individual axes.

3. Approach for a Single-Axis Sensor Setup

In nearly all modern machine tool calibration devices, optical techniques prevail [7,8]. The elaborated concept also primarily uses optical components for the following reasons:

- Optical sensors are able to provide a high resolution even for measurements concerning the largest existing machine tools.
- In contrast to setups with rigid components, e.g. glass scales, they are more adaptable to different machine tools and are reconfigurable.
- The decreasing size of active components, particularly emerging fibre-based interferometers, enables the complete setup to be sufficiently small for temporary or even permanent integration.

Both Renishaw with its *XM-60* system [9] and Automated Preicision (API) with the *XD-Laser* [10] offer commercial devices using optical principles for simultaneous calibration of linear axes in six degrees of freedom (6-DOF). While their measurement uncertainty is low enough for the implementation of the concept suggested in Figure 1, the cost of three systems is not viable. Moreover, these devices are designed for offline maintenenance use and provide very little flexibilty to adapt the measurement setup to the structure of the machine tool.

Chen et al. present a 6-DOF measurement setup using a single laser source, three fixed position sensing devices, two fixed beamsplitters, and one fixed mirror in combination with one additional mirror attached to the moving stage [11]. Li et al. show a 6-DOF surface encoder using a fixed sensor consisting of multiple optical components and a scale grating attached to the moving element [12]. Gao et al. designed a 6-DOF measurement method for X-Y stages using nine interferometers [13]. All three sensor assemblies can only partially be used for the discussed integration purposes, as their limited measurement range would reduce the applicability to small machine tools. For linear axes with larger travel ranges, Kuang et al. developed a 4-DOF system measuring straightness, yaw, and pitch error motions [14]. The combination of a semi-translucent mirror, beamsplitter, and position sensing devices for capturing angular error motions is very similar to the setup presented throughout this paper, but the measurement of straightness error motions follows an indirect principle using a corner cube retroreflector. The following approaches are regarded as appropriate for practical tests of the concept:

- Figure 4 shows the prototype implementation of a combination of a visible laser with two position sensing devices, placed in either the fixed base unit or the mobile sensor head. The linear positioning error motion is measured with the interferometer, while the camera in the sensor head can be used to measure the straightness error motions. Yaw and pitch are obtained by evaluating the displacement of the reflected beam on the camera in the base unit against the distance between both units. The inclinometer measures the roll error motion for non-vertical axes and can be of an arbitrary form, e.g. based on gravitational gauges. For vertical axes showing a significant roll error motion, the use of an optical principle is a possible alternative.
- The first approach can be modified to use only one position sensing device and three parallel laser beams used for interferometry to measure two angular error motions (pitch and yaw). Depending on the devices used, this variant may offer lower measurement uncertainties.
- The sensor setup proposed by Kuang et al. can be combined with an interferometer and a techique to measure roll error motions [14].
- Using multiple distributed sensor setups per direction of motion, the needed components change, e.g. the pitch of the gantry can be evaluated by measuring the travelled distance on both sides (see Figure 1).
- If one or more axes of the machine tool possess a built-in linear encoder capable of capturing positioning error motions, depending on the concept, the use of interferometry can be reduced or completely omitted and replaced by the encoder's information.

In all cases, the magnitude of the error motions can be determined from the sensor readings by applying the laws of reflection and refraction. Pitch and yaw error motions of the sensor head in the first approach (Figure 4) are evaluated through:

$$\varphi_{pitch} = \frac{1}{2} \frac{-u_{base} + c_{CB}}{l + c_I + a_{CB} - \left(1 - \frac{n_{ambient}}{n_{beamsplitter}}\right) \cdot d_{beamsplitter}} \tag{1}$$

$$\varphi_{yaw} = \frac{1}{2} \frac{-v_{base} + b_{CB}}{l + c_I + a_{CB} - \left(1 - \frac{n_{ambient}}{n_{beamsplitter}}\right) \cdot d_{beamsplitter}} \tag{2}$$

Here, u_{base} and v_{base} denote the displacement of the laser spot on the position sensing device in the base unit. The distance measured by the interferometer is referenced as l and $d_{beamsplitter}$ denotes the length of the beam splitter cube. The corresponding refractive indices are stated as $n_{ambient}$ and $n_{beamsplitter}$, whereas a_{CB}, b_{CB}, c_{CB}, a_{CM}, b_{CM}, and c_{CM} are calibration constants of the setup (see Figure 2). The yaw movement is obtained in the same way using the vertical beam displacement. Maintaining the naming convention and denoting the laser displacement on the position sensing device in the head unit by u_{head} and v_{head}, the horizontal (x) and vertical (y) straightness are calculated as:

$$x_{straightness} = u_{head} + a_{CM} + \varphi_{pitch} \cdot \left(c_{CM} - \left(1 - \frac{n_{ambient}}{n_{mirror}}\right) \cdot d_{mirror}\right) \tag{3}$$

$$y_{straightness} = v_{head} - b_{CM} + \varphi_{yaw} \cdot \left(c_{CM} - \left(1 - \frac{n_{ambient}}{n_{mirror}}\right) \cdot d_{mirror}\right) \tag{4}$$

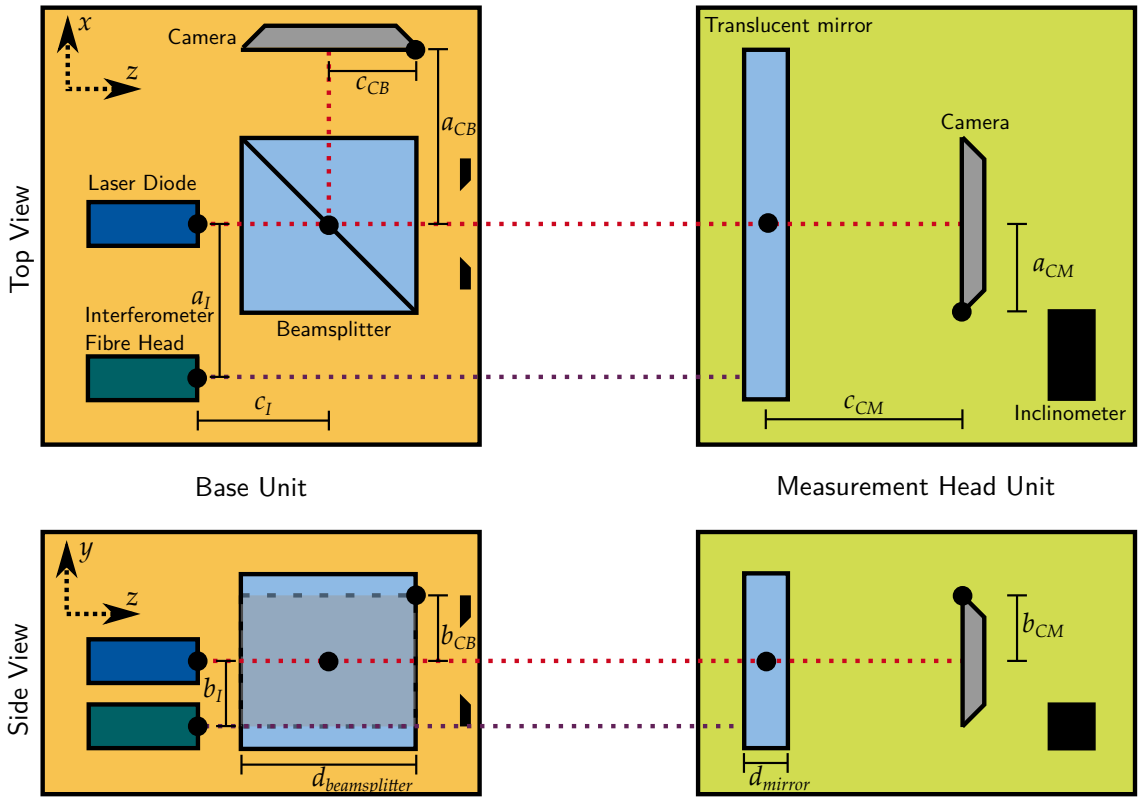

Figure 2. Sketch of the sensor setup proposed in Section 3 stating the names of the alignment constants used in Equations (1)–(4). The dots indicate the reference positions of the individual components. The prototype depicted in Figure 4 shows an implementation of the concept.

Linear positioning and roll error motions are trivially obtained from the interferometer and inclinometer readings. A virtual implementation of the sensor setup discussed in Section 5 is used to validate the mathematical formulation and propagation of uncertainties for different layouts.

For a compact base unit, the use of a fibre-based interferometer is advantageous. By only including the collimating fibre-head in the axis-integrated setup, the laser source and evaluation unit are placed outside the machine. One source can be used for multiple measurement lines and help reduce costs. Moreover, frequency modulating devices provide the possibility of absolute distance measurements, omitting the need for initial referencing of the setup [7].

4. Position Sensing Devices: Quadrant Detector vs. Industrial Cameras

The sensor setup presented in Section 3 as well as a wide range of metrological devices in general use position sensing devices to determine the lateral displacement between a laser beam and its target. During the first experiments, a Thorlabs *PDQ30C* [15] quadrant detector in combination with an infrared laser (1530 nm wavelength) beam was characterized and significant non-linear behaviour observed, leading to systematic measurement errors of several tens of micrometers.

This effect can be attributed to the principle of a quadrant detector assuming that the intensity is distributed uniformly across the profile of the incident beam. However, for most lasers the model of a Gaussian beam is more appropriate (Figure 3) [16]. The beam's respective spot size along the axis of propagation z is expressed as beam radius $w(z)$ following a hyperbolic relation:

$$w^2(z) := w_0^2 \left(1 + \left(\frac{z - z_0}{z_R}\right)^2\right) = w_0^2 + \theta_0^2 z^2 \tag{5}$$

$$w_0^2 := \frac{2 z_R}{k}, \qquad k = \frac{2\pi}{\lambda}, \qquad \theta_0 = \arctan\left(\frac{w_0}{z_R}\right) \tag{6}$$

In the above equations, λ denotes the wavelength. The beam waist w_0 is defined as the beam radius at the focal point $z = z_0$, and hence at its smallest extension. The divergence of the beam is characterized by the Rayleigh length z_R, which is the distance from the focal point at which the spot area has doubled and together with z_R defines the angle of divergence θ_0. With these parameters, the distribution of intensity across the beam profile can be expressed with a structure similar to a Gaussian probability distribution:

$$I(r, z) = I_0 \frac{w_0^2}{w^2(z)} \exp\left(-\frac{2r^2}{w^2(z)}\right) \tag{7}$$

The problem arising using quadrant detectors can be exemplified mathematically along one axis, assuming that the detector consists of two photosensitive halves with signals I_+ and I_-, and has a range of $\pm R$ around zero. Interpreting w as an effective beam radius along the detector axis, the signal S is proportional to the displacement of the beam's centre and can be computed from the difference of intensities distributed according to Equation (7):

$$S(x, w) \propto I_+ - I_- \propto \frac{1}{w^2} \int_0^R \exp\left(-\frac{2(s - x)^2}{w^2}\right) \mathrm{d}s - \frac{1}{w^2} \int_{-R}^0 \exp\left(-\frac{2(s - x)^2}{w^2}\right) \mathrm{d}s \tag{8}$$

$$\overset{-R \le x < R}{=} \frac{1}{w^2} \int_0^{2x} \exp\left(-\frac{2(s - x)^2}{w^2}\right) \mathrm{d}s \xrightarrow{\frac{x^2}{w^2} \ll 1} \frac{8x}{w^2} \overset{z \gg z_R}{\approx} \frac{8\pi}{z_R \cdot \lambda} \cdot \frac{x}{z^2} \tag{9}$$

Equation (8) unveils a clear non-linear relation between the beam position and the sensor signal, which may only be approximated linearly if the displacement is much smaller than the beam radius

and the latter is constant. For a typical laser, neither of these conditions hold, as the product of beam waist w_0 and angle of divergence θ is limited by the beam quality parameter M^2 [17]:

$$M^2 := w_0 \cdot \theta \cdot \frac{\pi}{\lambda} \geq 1 \tag{10}$$

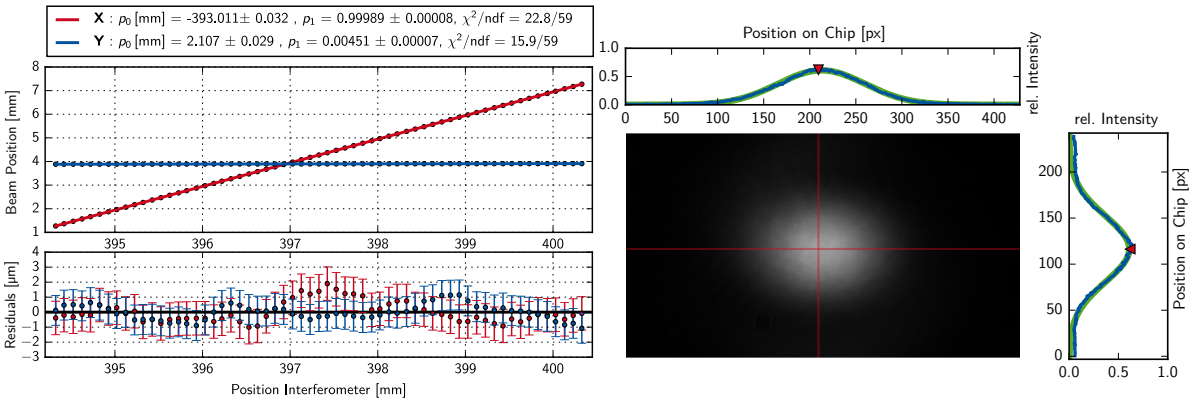

Figure 3. (**Left:**) Direct comparison of the displacement induced by a linear stage measured by an interferometer and the displacement of a laser beam profile captured by a camera. The respective parameters p_0 and p_1 are obtained through fitting a linear function by means of χ^2-minimization in both directions. (**Right:**) Camera image of a laser beam cross-section with profiles along the principal axes.

A measurement sequence to determine M^2 according to ISO 11146-1 was carried out for the *Premier LC laser diode* (635 nm wavelength) manufactured by Global Laser and used for the prototype setup in Section 6 (Appendix A) [18]. The results confirm the behaviour of a Gaussian laser beam with a quality parameter close to optimal ($M^2_{x'} = 0.93 \pm 0.09$ and $M^2_{y'} = 0.94 \pm 0.06$).

As an alternative, industrial charge-coupled-device (CCD) or complementary metal-oxide-semiconductor (CMOS) cameras in combination with neutral density filters capturing a digital image of the beam's cross-section [19] are investigated. A sample is shown in Figure 3. The image is regarded as histogram of a quantity following a bivariate Gaussian distribution. After removing noise, e.g. ambient light, by applying a threshold, the location and hence movement of the beam centre can be obtained by calculating the first algebraic moments of the histogram and converted into dimensional coordinates by multiplying with the pixel pitch of the camera [20]. The divergent beam radius imposes no problem as long as at least 95% of the beam cross-section is captured.

This idea was validated in an experimental setup using the aforementioned laser diode directed onto a Basler *piA2400-12gm* [21] camera with a pixel pitch of 3.45 µm. The camera was placed on a linear positioning stage orthogonally oriented to the beam direction, leading to a horizontal movement which was tracked using an Etalon *Absolute Multiline* interferometer [22]. Figure 4 shows the results of one run of the test series as a direct comparison of the displacement measured by both devices. An uncertainty ($k = 1$) of 1 µm is attributed to the interferometer and 1 µm is estimated as uncertainty for camera data. The uncertainties of the positioning stage do not influence the measurements as directly comparing the readings of camera and interferometer omit the need of the positioning stage's control data for evaluation.

The expected linear behaviour in horizontal and constant behaviour in vertical direction was confirmed by performing a chi-square minimization on the obtained data showing excellent agreement of assumed model and measured values (χ^2/ndf ≈ 0.5). Within a range of 7 mm, the displacement of the beam centre can be measured with an uncertainty ($k = 1$) of 1 µm + 1 µm/mm of the displacement range.

Hence the combination of visible laser diode and industrial camera is suited to quantify the movement of the sensor head via the beam displacement. Alongside, diode lasers and CCD/CMOS cameras are industrial-standard components and are available at moderate cost.

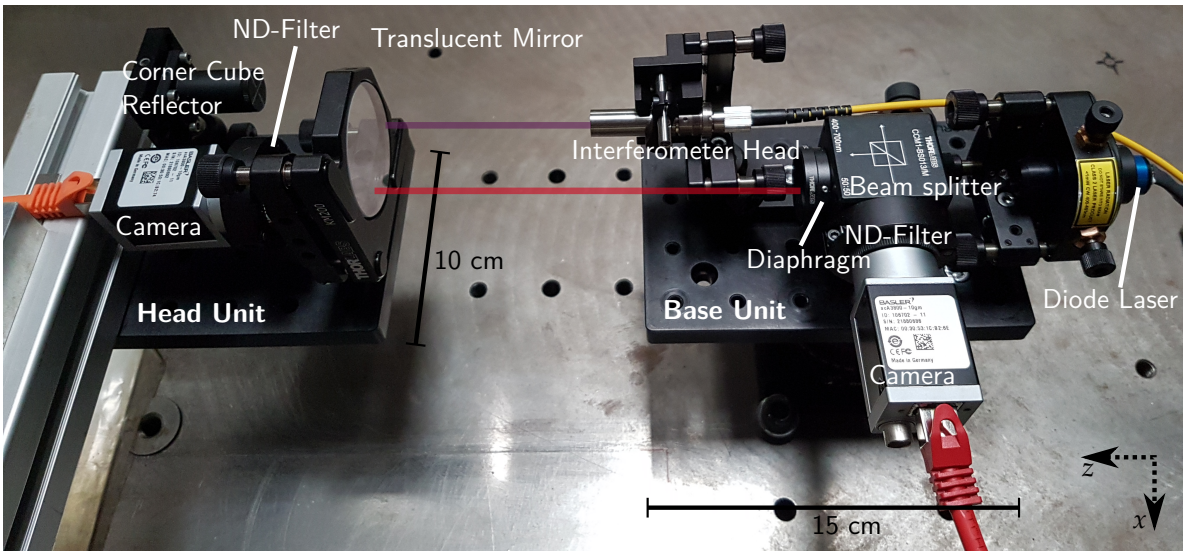

Figure 4. Photograph of the prototypes of base unit and measurement head unit setup with the components mentioned in Section 6. The parts were assembled using a modular fixture system manufactured by Thorlabs.

5. Simulation by Means of Raytracing

The development of a virtual sensor and machine tool setup allowing for numerical simulation of machine tool calibration measurements is motivated by the need for a validation of the established mathematical model. The existence of such a simulation in literature is unknown to the authors and is therefore regarded as novel.

As an approach for a virtual sensor, the measurement setup is interpreted as an optical system consisting of a common environmental medium representing ambient air, and homogeneous bodies with flat surfaces representing the optical components. Each surface holds a transmittance and reflectance coefficient either based on the Fresnel equations or its specific properties, e.g. a reflectance of nearly one for a mirror [23]. Refractive indices of air and bodies are calculated using Edlén and Sellmeier equations [24,25]. Position-sensing devices are modelled as absorbing surfaces, providing the coordinates of the intersection with the incident ray and its accumulated optical path as direct simulation outputs.

The complete composition of ambient medium and virtual optical components is handled as a scene for a raytracing algorithm [26,27]. For the simulation of the sensor's characteristics, different rays of light are propagated through the virtual setup. They are assumed to travel in a straight line, which has to be revised if temperature gradients or other environmental influences are to be taken into account [28]. In the present case, temperature, humidity, and pressure as input parameters are held constant during one simulation sequence, modelling an experiment in stabilized, e.g. acclimatized environmental conditions.

Origin, direction, intensity, and wavelength of the virtual light sources represent the initial conditions for the implemented raytracing procedure (Appendix B). When a ray intersects with a surface, it is split into a reflected and transmitted part with relative intensities according to the reflectance and transmittance coefficients (Equations (13) and (14)) [29]. The two parts are regarded as new rays originating from the intersection point with directions determined by the law of reflection (Equation (12)) and Snell's law (Equation (11)), respectively. The number of surfaces N_I hit by the

initial ray is incremented (Equation (15)) and the accumulated optical path is passed to the subsequent rays. Hence, at an intersection point the following equations hold [30]:

$$\mathbf{t}_\mathrm{T} = \frac{n_1}{n_2}\mathbf{t}_\mathrm{I} - \left(\frac{n_1}{n_2}\mathbf{t}_\mathrm{I}\cdot\mathbf{u} - \sqrt{1-\left(\frac{n_1}{n_2}\right)^2\left(1-(\mathbf{t}_\mathrm{I}\cdot\mathbf{u})^2\right)}\right)\mathbf{u} \tag{11}$$

$$\mathbf{t}_\mathrm{R} = \mathbf{t}_\mathrm{I} - 2\,(\mathbf{t}_\mathrm{R}\cdot\mathbf{u})\,\mathbf{u} \tag{12}$$

$$I_\mathrm{T} = T\cdot I_\mathrm{I} \tag{13}$$

$$I_\mathrm{R} = R\cdot I_\mathrm{I} \tag{14}$$

$$N_\mathrm{T} = N_\mathrm{R} = N_\mathrm{I} + 1 \tag{15}$$

In the above equations, $\mathbf{t}$ denotes the direction of a ray, I its intensity, and N its surface count. Vector $\mathbf{u}$ refers to the normal vector of the surface along the direction of transmittance and $n_{1,2}$ to the refractive indices on both sides in the same order. The indices I, R, and T correspond to incident, reflected, and transmitted rays, respectively. Finally, the raytracing procedure is continued with the two latter rays. Refraction and reflection are the only phenomena taken into account to determine the propagation direction and hence the mathematical model of the sensor established in Section 3 is not used as a priori information.

The formulation of a virtual machine tool can be simplified to two coordinate systems. These are a fixed system representing the machine frame, and a mobile coordinate system attached to the functional point which will be translated and rotated equivalently to the tool movement. The optical components are grouped into a stationary assembly described in the fixed coordinate system and a target assembly described in the mobile coordinate system. The virtual tool movement is described as the displacement and reorientation of the mobile coordinate system relative to the fixed one. From the perspective of raytracing, this corresponds to the generation of a new scene. Therefore, the simulation of the sensor is performed individually for each position in a virtual calibration cycle.

For the simulation of the sensor's behaviour, it is irrelevant if the tool movement is ideal or superposed with geometric errors. Hence, the total error motion is added to the movement of the functional point before the raytracing scene is generated. For this purpose, a pre-generated map of the axes' deviation in combination with the full-rigid-body model is used. The extension to a Monte-Carlo simulation consists of generating multiple scenes varying selected parameters according to a statistical distribution. On the computational side, all scenes are independent and the execution can be efficiently parallelized.

The virtual setup was used to validate the mathematical formulations stated in Section 3 and their according propagation of uncertainties. Moreover, systematic errors on the alignment constants a_{CB}, b_{CB}, c_{CB}, a_{CM}, b_{CM}, c_{CM}, and c_I were induced on purpose, confirming that c_{CB} and b_{CB} are most critical, as these constants neither cancel out when calculating error parameters of a linear axis according to ISO 230-1:2012(en) nor is their contribution to the total uncertainty budget after propagation negligible as for example for a_{CB}. Hence, a calibration procedure for c_{CB} and b_{CB} with an uncertainty ($k = 1$) of approximately 1 µm should be established. In the future, the virtual sensor will also be used to investigate the other hardware layouts introduced in Section 3 and different step diagonal machine tool calibration approaches [31].

6. Experimental Results of a Prototype Setup

According to the concept presented in Section 3, the authors implemented a prototype using the following components:

- The *Premier LC laser diode* (635 nm wavelength) manufactured by Global Laser and already used in Section 4 [18].
- Two Basler *acA3800-10gm* CMOS cameras with a pixel pitch of 1.67 µm and a frame rate of 10 Hz [32].

- Two Thorlabs *NE20A* neutral density filters with a transmission of 1% [33].
- A Thorlabs *CCM1-BS013/M* 50:50 cubic beamsplitter with an edge length of $d_{beamsplitter} = 25.4\,\text{mm}$ and anti-reflective coating [34].
- A Thorlabs *BSW30* 50:50 semi-translucent mirror with a thickness of $d_{mirror} = 8\,\text{mm}$ and an anti-reflective back side [35].
- An *IDS 3010* fibre-based interferometer manufactured by Attocube, operated at a wavelength of 1530 nm with an uncertainty ($k = 2$) of 1 µm/m over a 5 m displacement range with a bandwith up to 25 MHz [36,37].
- The inclinometer was omitted for the prototype as it is expected to operate independently. Thus, there is no experimental data for the roll error motion.

The entire setup is depicted in Figure 4. For validation purposes, the setup was mounted to a three-axis kinematic of gantry type without a built-in linear encoder, in parallel with a calibrated XD-Laser Precision from API [10] as a reference instrument while fixing both measurement heads on a common metal bar. The data was captured at equidistant stationary points along the gantry axis. The error parameters measured by the XD-Laser Precision instrument were corrected for the Abbe error introduced by the offset between both systems. The alignment constants a_{CB}, b_{CB}, c_{CB}, a_{CM}, b_{CM}, c_{CM} and c_I were calculated based on the dimensions of the component mountings used and the technical drawings provided by the cameras' manufacturer. Figure 5 shows a direct comparison of positioning (EXX), straightness (EYX, EZX), yaw (EAX), and pitch (EBX) error motions named adhering to ISO 230-1:2012(en) [2]. The error motions EXX along the axis itself are in very good agreement. The remaining differences are assumed to be due to different data from both interferometers' environmental sensor units entering the refractive index calculation. Moreover, the straightness error motions EYX and EZX agree very well bearing in mind the uncertainty budget and potential systematic errors arising from the Abbe error correction based on the data for the angular error motions EAX, EBX and ECX. The latter two unveil systematic differences between the measurements of the newly developed system and the API *XD-Laser* reference. In the case of EBX, an offset of up to 200 µrad between the API *XD-Laser's* measurements in forward and backward direction can be observed, which is not present in the data captured with the self developed sensor during the same calibration cycle of the kinematic. The authors assume that this behaviour is an artefact of the API instrument. The correlation, i.e. the qualitative similarity of both datasets, can still be regarded as very high. The same holds for the ECX error motion, although here the offset is attributed to a systematic error on the alignment constant c_{CB}, as similar behaviour has been observed during the simulated experiments in Section 5. An improved calibration procedure for the alignment constants is subject to current research within the project.

The response time of the system, which will determine degree of integration into the machine tool's control loop, has not been addressed yet. For the prototype the analysis of the beam profiles captured by the two cameras is carried out on an ordinary computer after transmitting the entire image through the Ethernet. This approach was chosen to first ensure the correct functionality of the sensor setup before optimizing latency and measurement rate. The latter will be limited by the acquisition rate of the camera chip used in the final setup, as the evaluation of the beam profiles can be shifted onto an field-programmable gate array (FPGA) directly connected to the imaging sensor.

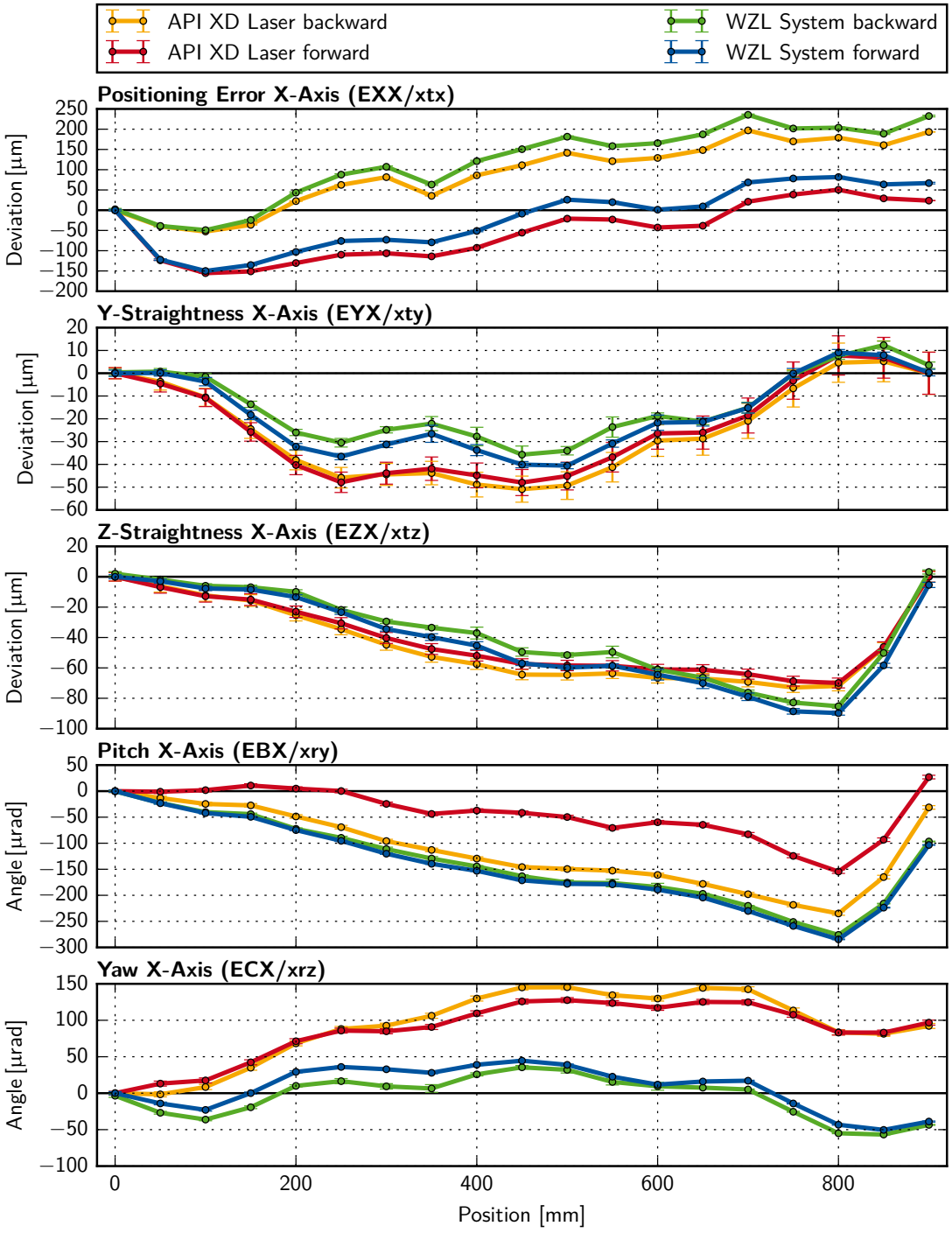

Figure 5. Error motion profiles simultaneously captured during competitive measurements on a three-axis gantry kinematic structure. Blue and green lines represent forward and backward direction data of the sensor setup discussed throughout this article, while red and yellow lines represent Abbe error-corrected reference data taken with the API *XD-Laser*. Uncertainties ($k = 2$) are mostly below 10 µm/µrad and hence are barely visible as error bars. Possible reasons for the differences between both datasets are discussed in Section 6.

7. Conclusions and Outlook

The presented concept of structure integrated sensors is suited to improving the time-efficiency of three-axis Cartesian machine tool calibration compared to current manual methods and enhances the potential of automation. The carried-out investigations sustain that laser diodes in combination with CCD/CMOS cameras, fibre-based interferometers, and inclinometers are eligible for a compact sensor setup that measures all six error motions of a rigid body component. Competitive measurements between the implemented prototype and a commercial machine tool calibration interferometer show good agreement with few remaining systematic errors, which will be further investigated by the authors.

At the same time, the sensor setup will be integrated into a machine tool of a gantry type serving as a permanent test carrier. Moreover, the machine tool's control has been adapted to process and compensate the error parameters measured by the sensor on-line automatically. As a consequence, the influence of vibrations and short-term environmental fluctuations within the machine tool on the stability of the measurement process have to be reevaluated. Once the development of the single-axis prototype is completed, it will be extended to the other axes of the machine tool.

Acknowledgments: The authors acknowledge financial support by DFG fund 1856/74-1 and DFG Cluster of Excellence *Integrative Production Technology for High-Wage Countries* (Project number: EXC 128).

Author Contributions: M.O. and R.H.S. conceived the concept of structure integrated machine tool calibration; B.M. and P.D. designed the single-axis sensor setup and carried out its experimental performance analysis; M.P. implemented the virtual sensor setup; All authors contributed to writing the paper.

Conflicts of Interest: The authors declare no conflict of interest. The founding sponsors had no role in the design of the study; in the collection, analyses, or interpretation of data; in the writing of the manuscript, and in the decision to publish the results.

Appendix A. ISO 11146-1 Beam Quality Parameter Estimation

To estimate the beam quality parameter M^2 defined in Equation (10) according to ISO 11146-1, the divergence of the beam radius across the axis of propagation according to Equation (5) is measured and the location of the focal point z_0, beam waist w_0, and the Rayleigh length z_R are determined by performing a least-squares-fit to the obtained data [17,38]. In the present case, the beam emitted by the laser diode unveils a simple astigmatic characteristic (visible as a rather elliptical beam profile), in which the analysis must be carried out individually for both principal components of the beam profile. This leads to two independent sets of parameters.

The experiment was carried out using almost the same setup as in Section 4, only changing the position and orientation of the laser diode such that the axis of propagation is parallel to the linear stage and the focal point is at approximately half of the travel range. For every 50 mm distance travelled, a sequence of 10 images is captured and the beam dimensions calculated by means of the second algebraic moments after applying a threshold of 5% to eliminate background noise. The uncertainty ($k = 1$) on the determined beam diameters is estimated to be 10%. Figure A1 shows the captured data and the two parabolic beam radius functions fitted by means of a χ^2-minimization. The Gaussian characteristic of the laser diode is confirmed by the experimental results which yield beam quality parameters of $M^2_{x'} = 0.93 \pm 0.09$ and $M^2_{y'} = 0.94 \pm 0.06$ in comparison to a quality parameter of $M^2 = 1$ for a pure Gaussian mode.

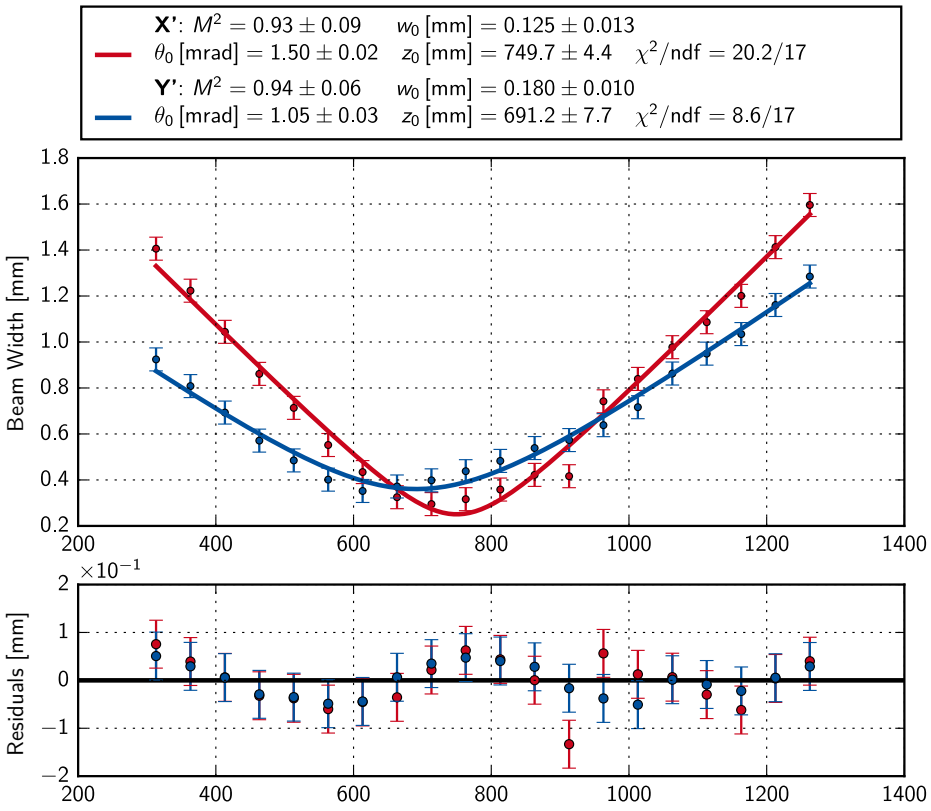

Figure A1. Results of a beam quality parameter measurement according to ISO 11146-1 for the diode laser used in the prototype setup. X′ (red) and Y′ (blue) denote the principal components of the bivariate Gaussian beam profile. The parameters w_0 and θ_0 correspond to beam waist and angle of divergence as defined in Equation (5).

Appendix B. Raytracing Algorithm

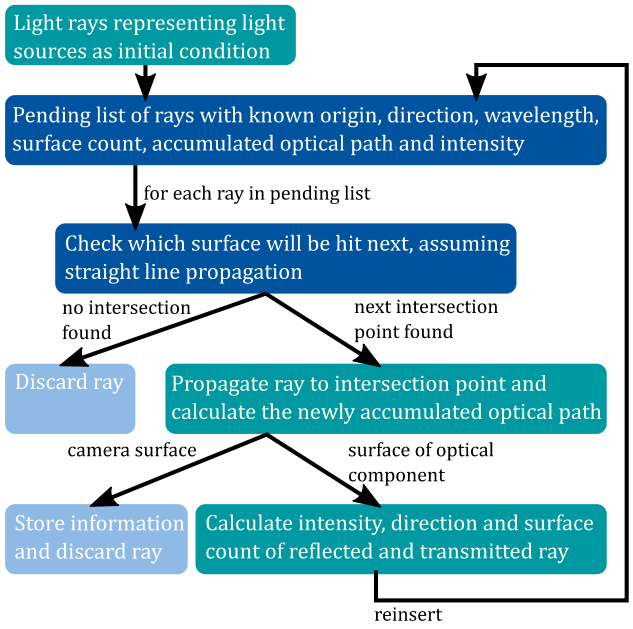

Figure A2. Flow chart of the raytracing procedure used for the simulation of the sensor setup in Section 5.

References

1. Schwenke, H.; Knapp, W.; Haitjema, H.; Weckenmann, A.; Schmitt, R.; Delbressine, F. Geometric error measurement and compensation of machines—An update. *CIRP Ann. Manuf. Technol.* **2008**, *57*, 660–675.
2. International Organization for Standardization. Test Code for Machine Tools—Part 1: Geometric Accuracy of Machines Operating under No-Load or Quasi-Static Conditions. Available online: https://www.iso.org/standard/46449.html (accessed on 26 January 2018).
3. Wang, C. Laser vector measurement technique for the determination and compensation of volumetric positioning errors. Part I: Basic theory. *Rev. Sci. Instrum.* **2000**, *71*, 3933.
4. Okafor, A.C.; Ertekin, Y.M. Derivation of machine tool error models and error compensation procedure for three axes vertical machining center using rigid body kinematics. *Int. J. Mach. Tools Manuf.* **2000**, *40*, 1199–1213.
5. Mayr, J.; Jedrzejewski, J.; Uhlmann, E.; Alkan Donmez, M.; Knapp, W.; Härtig, F.; Wendt, K.; Moriwaki, T.; Shore, P.; Schmitt, R.; et al. Thermal issues in machine tools. *CIRP Ann. Manuf. Technol.* **2012**, *61*, 771–791.
6. Lin, Y.; Shen, Y. Modelling of Five-Axis Machine Tool Metrology Models Using the Matrix Summation Approach. *Int. J. Adv. Manuf. Technol.* **2003**, *21*, 243–248.
7. Schmitt, R.H.; Peterek, M.; Morse, E.; Knapp, W.; Galetto, M.; Härtig, F.; Goch, G.; Hughes, B.; Forbes, A.; Estler, W.T. Advances in Large-Scale Metrology—Review and future trends. *CIRP Ann. Manuf. Technol.* **2016**, *65*, 643–665.
8. Mutilba, U.; Gomez-Acedo, E.; Kortaberria, G.; Olarra, A.; Yagüe-Fabra, J.A. Traceability of On-Machine Tool Measurement: A Review. *Sensors* **2017**, *17*, 1605.
9. Renishaw. XM-60 User Guide. Available online: http://resources.renishaw.com/en/details/user-guide-xm-60-multi-axis-calibrator--91595 (accessed on 14 February 2018).
10. API Services. XD Laser–Multi-Dimensional Laser Measurement System for CNC Calibration. Available online: https://apisensor.com/products/mth/xd-laser/ (accessed on 14 February 2018).
11. Chen, Y.T.; Lin, W.C.; Liu, C.S. Design and experimental verification of novel six-degree-of freedom geometric error measurement system for linear stage. *Opt. Lasers Eng.* **2017**, *92*, 94–104.
12. Li, X.; Gao, W.; Muto, H.; Shimizu, Y.; Ito, S.; Dian, S. A six-degree-of-freedom surface encoder for precision positioning of a planar motion stage. *Precis. Eng.* **2013**, *37*, 771–781.
13. Gao, Z.; Hu, J.; Zhu, Y.; Duan, G. A new 6-degree-of-freedom measurement method of X-Y stages based on additional information. *Precis. Eng.* **2013**, *37*, 606–620.
14. Kuang, C.; Feng, Q.; Zhang, B.; Liu, B.; Chen, S.; Zhang, Z. A four-degree-of-freedom laser measurement system (FDMS) using a single-mode fiber-coupled laser module. *Sensors Actuators A Phys.* **2005**, *125*, 100–108.
15. Thorlabs. PDQ30C—Quadrant Detector Sensor Head, 1000 to 1700 nm. Available online: https://www.thorlabs.com/thorproduct.cfm?partnumber=PDQ30C (accessed on 26 January 2018).
16. Reider, G.A. *Photonik*; Springer: Vienna, Austria, 2012.
17. Eichler, J.; Dünkel, L.; Eppich, B. Die Strahlqualität von Lasern—Wie bestimmt man Beugungsmaßzahl und Strahldurchmesser in der Praxis? *Laser Technol. J.* **2004**, *1*, 63–66.
18. Global Laser Ltd. Premier & Acculase Modulatable Laser Diode Modules. Available online: docs-europe.electrocomponents.com/webdocs/155d/0900766b8155d312.pdf (accessed on 26 January 2018).
19. Matsui, S.; Zhang, C. Alignment Method for 50m Distance Using Laser and CCD Camera. In Proceedings of the 7th International Workshop on Accelerator Alignment, Harima Science Park City, Japan, 11–14 November 2002; pp. 127–139.
20. International Organization for Standardization. Lasers and Laser-Related Equipment—Test Methods for Laser Beam Parameters—Beam Positional Stability. Available online: https://www.iso.org/standard/31690.html (accessed on 26 January 2018).
21. Basler AG. Basler Pilot Are Scan Cameras, 2016. Available online: https://www.baslerweb.com/fp-1489067453/media/downloads/documents/brochure/BAS1609_pilot_Brochuere_SAP0027_EN_web.pdf (accessed on 22 February 2018).
22. Etalon AG. Absolute Multiline Technology. Available online: http://www.etalon-ag.com/en/products/absolute-multiline-technology/ (accessed on 26 January 2018).

23. Demtröder, W. *Experimentalphysik 2: Elektrizität und Optik*, 6., überarb. u. akt. aufl; Springer: Heidelberg, Germany, 2013.
24. Edlén, B. The Refractive Index of Air. *Metrologia* **1966**, *2*, 71–80.
25. SCHOTT North America Inc. TIE-29 Refractive Index and Dispersion. Available online: http://www.schott.com/d/advanced_optics/02ffdb0d-00a6-408f-84a5-19de56652849/1.1/tie_29_refractive_index_and_dispersion_eng.pdf (accessed on 3 January 2018).
26. Pantazopoulos, J.S.; Tzafestas, S.G. An Efficient Algorithm for Ray Tracing. *J. Intell. Robot. Syst.* **2000**, *28*, 171–180.
27. Reif, J.H.; Tygar, J.D.; Yoshida, A. Computability and complexity of ray tracing. *Discret. Comput. Geom.* **1994**, *11*, 265–288.
28. Robson, S.; MacDonald, L.; Kyle, S.; Shortis, M.R. Close Range Calibration of Long Focal Length Lenses in a Changing Environment. In Proceedings of the ISPRS—International Archives of the Photogrammetry, Remote Sensing and Spatial Information Sciences, Prague, Czech Republic, 12–19 July 2016.
29. Roser, M. Modellbasierte und Positionsgenaue Erkennung von Regentropfen in Bildfolgen zur Verbesserung von Videobasierten Fahrerassistenzfunktionen. Available online: https://www.ksp.kit.edu/download/1000030435 (accessed on 22 Febraury 2018).
30. Schäfer, E. *Technische Optik: Mathematische und Physikalische Grundlagen*; Springer: Heidelberg, Germany, 1997.
31. Ibaraki, S.; Hata, T. A new formulation of laser step diagonal measurement—Three-dimensional case. *Precis. Eng.* **2010**, *34*, 516–525.
32. Basler AG. Basler Ace Are Scan Cameras. Available online: https://www.baslerweb.com/fp-1507878762/media/downloads/documents/brochure/BAS1708_ace_Brochure_SAP0025_EN_No30_web.pdf (accessed on 22 February 2018).
33. Thorlabs. NE20A Ø25 mm Absorptive ND Filter, SM1-Threaded Mount, Optical Density: 2.0. Available online: https://www.thorlabs.com/thorproduct.cfm?partnumber=NE20A (accessed on 26 January 2018).
34. Thorlabs. CCM1-BS014/M 30 mm Cage Cube-Mounted Non-Polarizing Beamsplitter, 700–1100 nm, M4 Tap. Available online: https://www.thorlabs.com/thorproduct.cfm?partnumber=CCM1-BS014/M (accessed on 26 January 2018).
35. Thorlabs. BSW30 Ø2in 50:50 UVFS Plate Beamsplitter, Coating: 600–1700 nm, t = 8 mm. Available online: https://www.thorlabs.com/thorproduct.cfm?partnumber=BSW30 (accessed on 26 January 2018).
36. Karrai, K. Verfahren und Vorrichtung zur Positionserfassung. EP2045572A1. Available online: https://patents.google.com/patent/EP2045572A1 (accessed on 26 January 2018).
37. Attocube Systems. IDS3010/SMF: Displacement Sensing for Industry & Synchrotron, 2017. Available online: http://marketing.attocube.com/acton/attachment/4434/f-0322/0/-/-/-/-/IDS3010.pdf (accessed on 22 Febraury 2018).
38. DIN Deutsches Institut für Normung e. V. Laser und Laseranlagen—Prüfverfahren für Laserstrahlabmessungen, Divergenzwinkel und Beugungsmaßzahlen Teil 1: Stigmatische und Einfach Astigmatische Strahlen. Available online: https://www.beuth.de/de/norm/din-en-iso-11146-1/74054387 (accessed on 22 February 2018).